Effect of schmidt number on the structure and propagation of density currents

Thomas Bonometti, S. Balachandar

Thomas Bonometti · S. Balachandar

Effect of Schmidt number on the structure and propagation of density currents

Abstract The results of a numerical study of two- and three-dimensional Boussinesq density currents are described. They are aimed at exploring the role of the Schmidt number on the structure and dynamics of density driven currents. Two complementary approaches are used, namely a spectral method and a finite-volume interface capturing method. They allow for the first time to describe density currents in the whole range of Schmidt number $1 \leq Sc \leq \infty$ and Reynolds number $10^2 \leq Re \leq 10^4$. The present results confirm that the Schmidt number only weakly influences the structure and dynamics of density currents provided the Reynolds number of the flow is large, say of $O(10^4)$ or more. On the contrary low- to moderate-Re density currents are dependant on Sc as the structure of the mixing region and the front velocities are modified by diffusion effects. The scaling of the characteristic density thickness of the interface has been confirmed to behave as $(ScRe)^{-1/2}$. Three-dimensional simulations suggest that the patterns of lobes and clefts are independent of Sc. In contrast the Schmidt number is found to affect dramatically (1) the shape of the current head as a depression is observed at high-Sc, (2) the formation of vortex structures generated by Kelvin–Helmholtz instabilities. A criterion is proposed for the stability of the interface along the body of the current based on the estimate of a bulk Richardson number. This criterion, derived for currents of arbitrary density ratio, is in agreement with present computed results as well as available experimental and numerical data.

Keywords Density currents · Gravity currents · Buoyancy driven flows · Mixing · Spectral methods · Finite volume methods

PACS 47.11.-j · 47.20.Bp · 47.55.P- · 92.10.Lq

1 Introduction

Density currents are mainly horizontal flows that are driven by lateral pressure gradient induced by density difference between the current and the surrounding fluid. These flows are encountered in various geophysical, environmental and safety problems such as thunderstorm fronts, volcanic eruptions, oil spills on the ocean, snow avalanches and fires in enclosed structures [1,16,36]. These density currents can be produced with density differences ranging from a fraction of a percent (e.g. oceanic currents with inhomogeneous salinity or

T. Bonometti (✉) · S. Balachandar
Department of Mechanical and Aerospace Engineering, University of Florida, Gainesville, FL 32611, USA
E-mail: bonomett@ufl.edu
E-mail: bala1s@ufl.edu

temperature) to large values (e.g. dam break flows). Density currents can be considered as Boussinesq flows as long as the density ratio does not exceed 1.2 approximately [13,17]. Recently Huppert [22] provided a review of the rich physical problems related to density currents.

The degree to which the heavy and light fluids mix can be an important factor in determining the structure and dynamics of the current. Mixing at the macroscale is due to interfacial instability, while mixing at the molecular level is controlled by diffusivity of the agent responsible for density difference. In gases and liquids, thermal and concentration diffusivities show wide variation. For example, the Schmidt (or Prandtl) number for thermal diffusivity in air is around 0.7, while in water it is about 7.0. Here the Schmidt number (Sc) is defined as the ratio between the kinematic viscosity ν and the molecular diffusivity K of the fluids, i.e. $Sc = \nu/K$. In contrast, the Schmidt number for salt and several other solvents in water is about 700. If the density difference is due to a suspension of fine particles then the effective Schmidt number is typically large and often a complex function of local shear and particle concentration.

There are situations where the two fluids are molecularly immiscible, as in the case of an oil slick spreading on water or the flood of water into the ambient air after a dam break. The Schmidt number tends to infinity in these cases and mixing of the different fluids is only at the macro-scale through interfacial instability and turbulence. Thus, Schmidt numbers ranging from less than one to very large values tending to infinity are of practical interest. In the case of density currents involving immiscible fluids, density and viscosity ratio between the two fluids and surface tension effects also play a role.

Two and three-dimensional simulations have been performed for Boussinesq planar density currents at moderate Reynolds numbers [9,13,18,25,29]. They provide detailed information on the propagation speed of the current, the three-dimensional lobe and cleft structure of the head, and the turbulent structure of the body. All these simulations use the assumption that the molecular diffusivity K and the kinematic viscosity ν of the fluids are of the same order, i.e. the Schmidt number $Sc = O(1)$. Necker et al. [28] performed a number of test calculations for different values of Sc and observed the flow to be nearly independent of Sc as long as Sc was not much smaller than one. Birman et al. [3] indicated that the influence of Sc in the range 0.2–5 to be quite small.

Numerical approaches based on variable density single fluid formulation are typically limited to modest values of Schmidt number. While the Reynolds number (Re) controls the smallest length scale associated with the velocity field, $ScRe$ controls the smallest length scale associated with the concentration field. Thus, for large Sc unattainably fine grids are required to resolve the sharp concentration interface, while the flow itself does not require such resolution. As a result the Schmidt number in these simulations is typically limited to less than 10. Only numerical approaches that are designed to resolve sharp interfaces can handle nearly immiscible fluids. They however are not well suited for studying density currents at $O(1)$ Sc. As a result an extensive study over a wide range of Sc from $O(1)$ to very large values has not been performed so far, and the detailed influence of the Schmidt number on the structure and dynamics of density currents remains an open question. Interestingly, the hydraulic theories of density currents ignore molecular diffusivity and thus consider the immiscible limit [2,34,38].

Here we attempt to deepen our understanding of the influence of the Schmidt number on the structure and dynamics of Boussinesq flows through numerical simulations. We present two- and three-dimensional computational results of lock–exchange density currents for various Reynolds numbers. Two different numerical techniques are employed in this work, namely, a spectral method and a finite-volume method, allowing us to investigate the role of the Schmidt number on density currents over a wide range of Sc. We describe in Sect. 2 the computational approaches and illustrate the accuracy of the numerical methods for density currents. The influence of the Schmidt number on currents of various Reynolds number is analyzed in Sect. 3. In this section the effect of Sc on the three-dimensionality of the current is also addressed. A summary of the main results is given in Sect. 4.

2 Numerical formulation

The physical configuration of the density currents to be considered here is shown in Fig. 1. Initially, a slab of heavy fluid of density ρ_H (shown in Fig. 1 as the shaded region) is separated from the light fluid of density ρ_L. The heavy fluid is initially of half-width x_0 along the flow direction and extends over the entire height H of the channel (lock–exchange configuration).

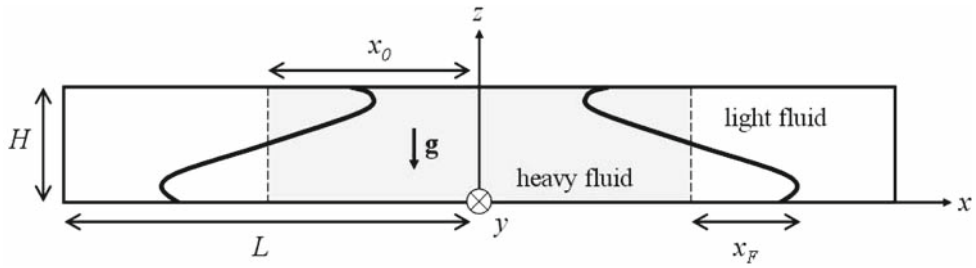

Fig. 1 The physical configuration and nomenclature used in this work. The *dotted line* represents the initial separation between fluids. The *thick line* represents the interface at later times. The whole domain $2L \times H$ is computed in the spectral code while the right-half side of the domain $L \times H$ is computed in the finite-volume code

2.1 Basic equations

If we assume the two fluids to be Newtonian, incompressible and miscible with no phase change, their evolution is then described using the one-fluid formulation of the Navier–Stokes equations, namely

$$\nabla \cdot \boldsymbol{u} = 0, \tag{2.1}$$

$$\rho \frac{\partial \boldsymbol{u}}{\partial t} + \rho\, \boldsymbol{u}.\nabla \boldsymbol{u} = -\nabla p_{\text{tot}} + \rho\, \boldsymbol{g} + \nabla \cdot \left[\mu \ \left(\nabla \boldsymbol{u} + (\nabla \boldsymbol{u})^t\right), \right], \tag{2.2}$$

where $\boldsymbol{u}$, p_{tot}, ρ and μ are the local velocity, total pressure, density and dynamic viscosity in the flow, respectively and $\boldsymbol{g}$ denotes gravity. In the case of miscible fluids, the local density obeys

$$\frac{\partial \rho}{\partial t} + \boldsymbol{u}.\nabla \rho = K\, \nabla^2 \rho, \tag{2.3}$$

where the molecular diffusivity K is taken to be constant. In the following, we assume the viscosity to be constant and the same for both fluids. We consider the dynamic pressure $p = p_{\text{tot}} + \rho_L g z$ instead of the total pressure (z being the spatial coordinate parallel to the gravity vector), and choose H as length scale, $U = \sqrt{g'H}$ as velocity scale and H/U as time scale (g' is the reduced gravity defined as $g' = g(\rho_H - \rho_L)/\rho_L$). The dimensionless density and pressure are given by

$$\tilde{\rho} = \frac{\rho - \rho_L}{\rho_H - \rho_L}, \quad \text{and} \quad \tilde{p} = \frac{p}{\rho_L U^2} \tag{2.4}$$

Any variable with a tilde on top is to be understood as dimensionless. The dimensionless form of (2.1)–(2.3) read

$$\frac{\partial \tilde{u}_k}{\partial \tilde{x}_k} = 0 \tag{2.5}$$

$$(1 + \varepsilon\tilde{\rho}) \left[\frac{\partial \tilde{u}_i}{\partial \tilde{t}} + \tilde{u}_k \frac{\partial \tilde{u}_i}{\partial \tilde{x}_k}\right] = \tilde{\rho} e_i^g - \frac{\partial \tilde{p}}{\partial \tilde{x}_i} + \frac{1}{Re} \frac{\partial^2 \tilde{u}_i}{\partial \tilde{x}_k \partial \tilde{x}_k}, \tag{2.6}$$

$$\frac{\partial \tilde{\rho}}{\partial \tilde{t}} + \tilde{u}_k \frac{\partial \tilde{\rho}}{\partial \tilde{x}_k} = \frac{1}{ScRe} \frac{\partial^2 \tilde{\rho}}{\partial \tilde{x}_k \partial \tilde{x}_k}. \tag{2.7}$$

Three dimensionless parameters have been introduced in (2.5)–(2.7) namely the Reynolds number, the Schmidt number and the parameter ε defined as

$$Re = \frac{UH}{\nu} = \frac{\sqrt{g'H}H}{\nu}, \quad Sc = \frac{\nu}{K}, \quad \text{and} \quad \varepsilon = \frac{\rho_H - \rho_L}{\rho_L}. \tag{2.8}$$

2.2 The two computational approaches

In this work we have employed two different numerical techniques: a fully de-aliased pseudo-spectral code [10] and a finite-volume/volume-of-fluid method with no interface reconstruction [5]. The spectral code was used to simulate currents with moderate Schmidt number while the finite-volume code was used for high-Sc. This allows us to explore the range of parameters $10^2 \leq Re \leq 10^4$ and $1 \leq Sc \leq \infty$.

2.2.1 The spectral code

In the spectral code, Fourier expansions are employed for the flow variables along the horizontal directions ($\tilde{x}$ and $\tilde{y}$). In the inhomogeneous vertical $\tilde{z}$-direction a Chebyshev expansion is used with Gauss-Lobatto quadrature points [10]. Details on the implementation of this numerical scheme can be found in Cortese and Balachandar [12].

Periodic boundary conditions are enforced along the horizontal directions and as shown in Fig. 1 the computational domain is a rectangular box of size $2L \times H$. The box is typically taken to be very long along the streamwise direction in order to allow free unhindered development of the current. At the top and bottom walls, no-slip and zero-gradient conditions are enforced for velocity and density, respectively. The initial density is smoothly varied from 0 to 1 over a thin region located at the interface [3,8]. The flow is started from rest with a minute random disturbance prescribed in the density field.

In the present work, only two-dimensional computations are performed with this code (three-dimensional examples can be found in Cantero et al. [8]). We employ a $1{,}024 \times 80$ grid in a $32H \times H$ domain ($L = 16H$) for all Re except $Re = 10^4$ for which a $4{,}000 \times 200$ grid in a $64H \times H$ domain is used, as in Birman et al. [3]. The numerical resolution for each simulation is selected to have between 4 and 6 decades of decay in the energy spectrum for all the variables. The time step is selected to produce a Courant number smaller than 0.5. In the spectral code, the value of the parameter ε in Eq. (2.6) is set to zero.

2.2.2 The finite-volume code

The second numerical technique is a finite-volume/volume-of-fluid method with no interface reconstruction. Equations (2.5)–(2.7) are solved using the JADIM code originally developed for gas–liquid flows capable of accurately capturing the dynamics of flows with high density ratios [5,6]. In this approach, the equation of evolution of the density is chosen to be hyperbolic, i.e. the right-hand side of Eq. (2.7) is zero. Although no physical diffusivity is introduced in the advection of $\tilde{\rho}$, the numerical thickness of the interface is not strictly zero as it is typically resolved over three grid cells [6]. This is equivalent to using a Schmidt number sufficiently large that the product $ScRe$ in the right-hand side of Eq. (2.7) is much greater than one (denoted as $Sc \to \infty$ throughout this paper). An effective Schmidt number can be estimated, which depends on the degree of spatial resolution. The effective Schmidt number for the spatial resolutions used here is estimated to be of $O(10^3)$ (see Appendix).

The transport equation of the density is solved using a modified version of the transport scheme proposed by Zalesak [39]. The overall algorithm is second-order accurate in both time and space. Details on the algorithms as well as validation of the code may be found in Bonometti and Magnaudet [6].

A symmetry free-slip boundary condition is used along the $x = 0$ plane, and thus the computational domain used with the finite-volume code is only half that used for the spectral code (i.e. the domain size is $L \times H$). At the top and bottom walls, no-slip and zero concentration gradient conditions are imposed. The initial density $\tilde{\rho}$ is defined as 1 for $x \leq x_0$ and 0 for $x > x_0$ and the fluid is initially at rest. Two and three-dimensional computations performed with this code are presented here. As for the two-dimensional simulations, we use a $1{,}600 \times 160$ grid in a $25H \times H$ domain ($L = 25H$) for all Re except $Re = 10^4$ for which a 2400×240 grid is used. The details of the 3D simulations are provided in Sect. 3.5. Since the finite-volume code is written so as to treat fluids of arbitrary density contrast, we cannot strictly impose the value of the parameter ε in Eq. (2.6) to be zero, therefore ε is set to 0.01 in order for the currents to be considered as Boussinesq.

2.3 Preliminary tests and validation

The present two techniques have been used in the past and validated for various problems. Resolution requirements of the spectral code in the Boussinesq limit have been well established [8,9]. Also the energy spectra in

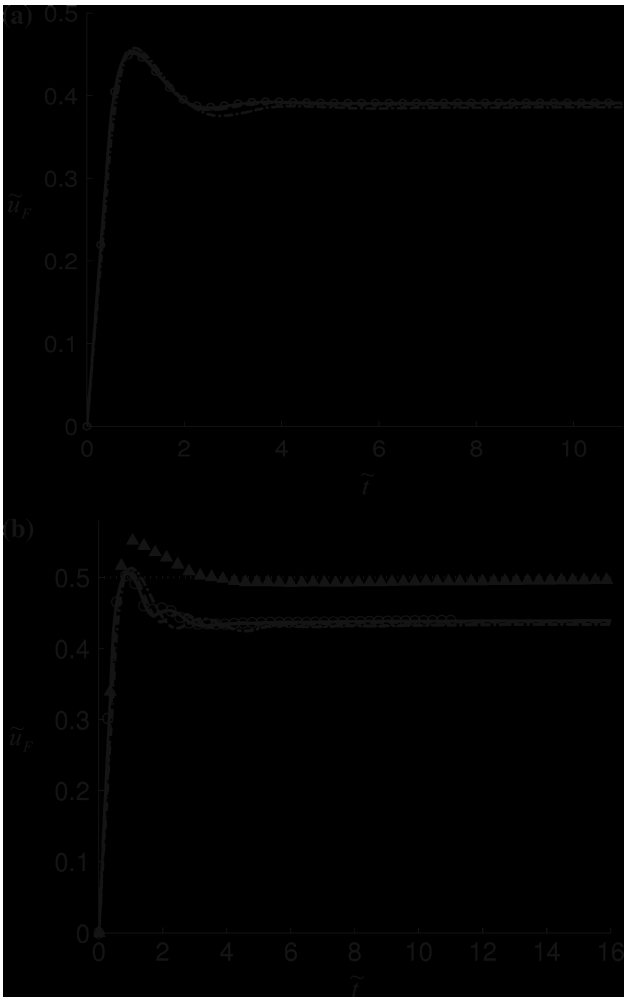

Fig. 2 Time evolution of the front velocity of the $Sc \to \infty$ density current at different grid resolutions. **a** $Re = 10^3$; **b** $Re = 10^4$. *Dashed-dotted line:* 416×80. *Dashed line:* 832×160. *Solid line:* $1{,}248 \times 240$. *Circles:* $1{,}664 \times 320$. *Dotted line:* Benjamin's theory. *Triangles:* simulation with free-slip boundary conditions (grid 832×160). Note that for $Re = 10^3$, the velocity curves of the last three grid resolutions are almost indistinguishable

the present spectral simulations have been verified to show several decades of decay and thereby ensuring the adequacy of resolution.

The finite-volume method has been shown to reproduce correctly the dynamics of gas–liquid flows at low to moderate Re [5,6]. In order to establish the accuracy of the finite volume code in the context of density currents here we present a resolution test. We consider a lock–exchange flow between two non-diffusive fluids of density ratio $\rho_H/\rho_L = 1.01$. Two different Reynolds numbers of 10^3 and 10^4 are considered. The longitudinal domain size is $L = 13H$ and the location of the initial lock is at $\tilde{x}_0 = 6.5$. No-slip boundary conditions are imposed at the top and bottom walls. The computational resolution was increased four fold with the following grids: 416×80, 832×160, $1{,}248 \times 240$ and $1{,}664 \times 320$, which will be referred to as $R1$, $R2$, $R3$ and $R4$, respectively.

The time evolution of the front velocity at the two different Reynolds numbers for the different grid resolutions is shown in Fig. 2. In all cases a slumping phase with a near constant front velocity is observed and the approach to constant velocity is oscillatory. For $Re = 10^3$ the constant velocity obtained with grids $R1$, $R2$, $R3$ and $R4$ are 0.386, 0.390, 0.391 and 0.391, respectively. For $Re = 10^4$ the constant velocity obtained with grids $R1$, $R2$, $R3$ and $R4$ are 0.433, 0.437, 0.439 and 0.439, respectively. With increasing resolution the constant front velocities show convergence, but are 22 and 12% lower than Benjamin [2] prediction for $Re = 10^3$ and $Re = 10^4$, respectively. The difference in the higher Re case can be attributed to the effect of the top and bottom no-slip walls, which are not taken into account in the theory [18]. Indeed, also plotted in Fig. 3b is

Table 1 Evolution of some quantities with the spatial resolution in the cases $Re = 10^3$ and $Re = 10^4$ (finite-volume code, $Sc \to \infty$)

Mesh size	$\tilde{u}_F^{\text{peak}}$	$\tilde{t}^{\text{peak}}$	$\tilde{u}_F^{\infty}$	$\tilde{E}_{\text{d}}$
$Re = 10^3$				
$R1$ (416 × 80)	0.458	0.983	0.386	0.000481
$R2$ (832 × 160)	0.454	0.935	0.390	0.000518
$R3$ (1,248 × 240)	0.452	0.931	0.391	0.000531
$R4$ (1,664 × 320)	0.452	0.931	0.391	0.000535
$Re = 10^4$				
$R1$ (416 × 80)	0.513	1.030	0.433	0.000115
$R2$ (832 × 160)	0.509	0.942	0.437	0.000149
$R3$ (1,248 × 240)	0.506	0.911	0.439	0.000167
$R4$ (1,664 × 320)	0.505	0.910	0.439	0.000179

$\tilde{u}_F^{\text{peak}}$ Maximum value of the front velocity, $\tilde{t}^{\text{peak}}$ time of maximum front velocity, $\tilde{u}_F^{\infty}$ constant front velocity, $\tilde{E}_{\text{d}}$ energy dissipation measured at time $\tilde{t} = 10$, and scaled by the initial potential energy

the result of a simulation with free-slip boundary conditions for the resolution $R2$, and $Re = 10^4$. It is clear that at sufficiently high Reynolds number with free-slip boundary condition Benjamin's prediction can be recovered. We note in passing that Rottman and Simpson [32] reported a similar discrepancy of 10% between their experimental results and Benjamin's prediction. Also Härtel et al. [18] report front velocity to within 2% with the theoretical prediction, for a current spreading on a free-slip bottom boundary. As can be observed in Fig. 2, the front velocity reaches a peak before approaching the constant velocity in the slumping phase. Table 1 presents the peak front velocity, the time instance of the peak and total dissipation within the domain for the different grid resolutions. The slow approach to convergence illustrates the need for higher resolution with increasing the Reynolds number.

Density contours at time $\tilde{t} = 11.3$ are plotted in Fig. 3 for the $Re = 10^4$ case at three different grid resolutions. The large scale features of the flow, i.e. the front position and the roll-up of the interface into the main vortex structures, are similar at the different resolutions. However, small scale structures continue to become finer with increased resolution. This behavior is well evident in the thickness of the interface at the head of the current as captured by the density contours of value from 0.05 to 0.95. The thickness of the interface continues to decrease with increasing resolution. With no explicit diffusion in the concentration equation being solved, the numerical resolution of the sharp interface across three grid cells provides the effective diffusivity. The location of the rolled-up vortices and the precise manner of interaction between them shows some variation between the different resolutions. These differences are due to the chaotic nature of the interfacial instability and the roll up process at $Re = 10^4$. As the heavy and light fronts propagate to the right and left, respectively, new vortices roll up at the interface close to the propagating fronts. The onset of roll up is sensitive to the details of the initial disturbance and to the round off errors arising from the different discretizations. As a result, at the time instance shown in Fig. 3 differences can be observed in the state of the incipient vortex roll

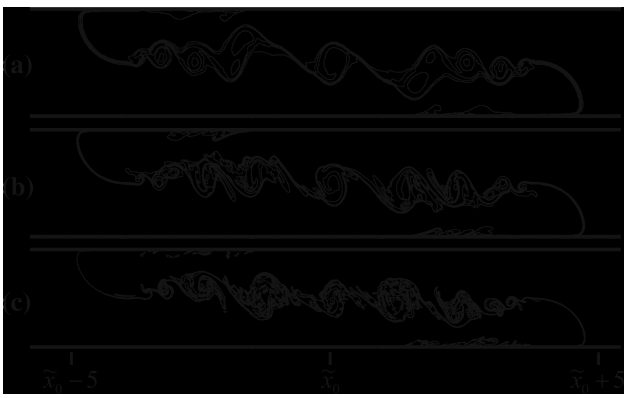

Fig. 3 Contours of $\tilde{\rho}$ obtained with the finite-volume method ($Sc \to \infty$) at $Re = 10^4$. Results are for $\tilde{t} = 11.3$ with grids **a** 416 × 80; **b** 832 × 160; **c** 1,664 × 320. The values of the plotted contours are $\tilde{\rho} = 0.05 - 0.275 - 0.5 - 0.725 - 0.95$. Images are vertically stretched by a factor 2

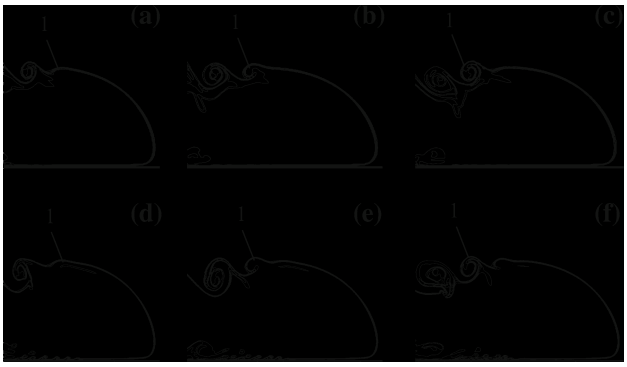

Fig. 4 Snapshots of the head at different time instants obtained with the finite-volume method ($Re = 10^4$, $Sc \to \infty$): **a–c** $1{,}248 \times 240$ grid and **d–f** $1{,}664 \times 320$ grid. The time difference between snapshots is constant and the same for both grids ($\Delta\tilde{t} = 0.56$). The values of the plotted contours are $\tilde{\rho} = 0.05, 0.275, 0.5, 0.725$ and 0.95. Images are vertically stretched by a factor 2. Note that the position of the current's front at a given time instance is identical for all the spatial resolutions

up. These subtle differences in the initial roll up process persist as differences in the precise location of the rolled-up vortices and their interaction.

A close examination of the incipient roll up close to the current head, however, shows that this process is statistically grid independent. This is demonstrated in Fig. 4, where a close view of the interfacial roll up close to the heavy front at three different time instances for the two highest resolutions are shown. Note that frames (a) and (d) are not at the same time instance. The time instances have been slightly shifted in order to extract incipient vortices at nearly similar stage in their development. The non-dimensional time gap between frames (a), (b) and (c) is chosen to be the same as between frames (d), (e) and (f). It can be observed that although the periodic initiation of roll up is sensitive and shows subtle variation in timing between the different resolutions, the process of interfacial roll up, vortex formation and interaction is robust and grid independent. The above complexity seen in the concentration field is largely mitigated in the velocity field owing to the finite Re. This can be verified in the convergence of front velocity and the energy dissipation statistics shown in Table 1.

3 Results

3.1 Interface thickness

We consider first the case of a low-Re Boussinesq density current for $Re = 10^2$. In Fig. 5 we present contours of $\tilde{\rho}$ at $\tilde{t} = 12.7$ obtained for four different Schmidt numbers, namely $Sc = 1$, 10, 10^2, and ∞. At this low Reynolds number, there is no vortex roll up of the interface whatever the Schmidt number. The most striking difference is in the thickness of the interface, while its shape remains nearly the same. Although subtle, another difference is in the small depression that can be observed close to the head of the front at high Sc. The thickness of the interface measured normal to the interface along the body of the current is expected to vary according to $h_\alpha/H \sim (ScRe)^{-1/2}$. This scaling relation can be derived from an order-of-magnitude analysis of the terms in the continuity equation (2.3), and by balancing the strain and diffusion effects (see e.g. [4,24]). The thickness of the interface can be defined as the normal distance measured between contours of $\tilde{\rho} = \alpha$ and $\tilde{\rho} = 1 - \alpha$, and thus can be expected to depend on the choice of α. In the Appendix (Fig. 17) it is shown that the above scaling relation for the interface thickness is satisfied to within 4% accuracy, independent of the choice α.

Density currents at four different Reynolds numbers, namely $Re = 10^2$, 317, 10^3, 10^4, are shown in Fig. 6. Only the results for $Sc = 1$ and $Sc \to \infty$ are shown so that comparisons can be made between these two limiting cases. As already observed in Fig. 5, no vortex structure is observed at the lowest Re considered (cases c and d of Fig. 6) but above a critical Re, the interface becomes unstable with growing Kelvin–Helmholtz instability, resulting in the roll up of the interface into coherent vortex structures and leading to strong convective mixing. These vortex structures are observed at $Re = 10^3$ and 10^4 in the cases $Sc = 1$ and $Sc \to \infty$, respectively. The characteristic thickness of the interface along the body of the current is not constant anymore but varies with the local flow structures.

A quantitative comparison of the topology of the interface is provided in Fig. 7. Based on the work of Pawlak and Armi [30], who measured mixing and entrainment in developing stratified currents, we estimate

Fig. 5 Contours of $\tilde{\rho}$ at $\tilde{t} = 12.7$ ($Re = 10^2$). Results for **a** $Sc = 1$, **b** $Sc = 10$, **c** $Sc = 10^2$ and **d** $Sc \to \infty$. Frames **a** to **c** are from the spectral code for which the grid resolution is $1{,}024 \times 80$ on a $32H \times H$ over-all domain. Frame **d** is from the finite-volume code for which the grid resolution is $1{,}600 \times 160$ on a $25H \times H$ domain. The values of the plotted contours are $\tilde{\rho} = 0.05 - 0.275 - 0.5 - 0.725 - 0.95$. Images are vertically stretched by a factor 3.33

an averaged density thickness $\tilde{\delta}_\rho$ as the inverse slope of the best-fit line through the normalized density profiles between 15 and 85% values,

$$\tilde{\delta}_\rho = \frac{1}{L_\mathrm{b}} \int_{L_\mathrm{b}} \left(\left. \frac{\partial \tilde{\rho}}{\partial \tilde{z}} \right|_{0.15 \le \tilde{\rho} \le 0.85} \right)^{-1} \mathrm{d}x. \tag{3.1}$$

The integral corresponds to spatial averaging along the horizontal direction inside the body of the current (the length of the body of the current is referred to as L_b). Here the body of the current is defined to exclude the head of the heavy and light fronts. The head region is taken to be one dimensionless height from the front position and thus the average is only over the interior of the interface.

The temporal evolution of $\tilde{\delta}_\rho$ is plotted in the inset of Fig. 7 for four cases: two Schmidt numbers of $Sc = 1$, $Sc \to \infty$ and two Reynolds numbers of $Re = 317$ and $Re = 10^4$. In the two lower dashed curves, which correspond to $Sc \to \infty$, the averaged density thickness increases at early times to reach a plateau of nearly constant value for $\tilde{t} > 8$. In the two upper curves, which correspond to $Sc = 1$, $\tilde{\delta}_\rho$ progressively increases during the entire period of spreading and the increase is more significant for the smaller Re case. The time-averaged value of $\tilde{\delta}_\rho$ (averaged over the range $8 \le \tilde{t} \le 20$) is plotted for currents of varying Re and Sc in Fig. 7. The time-averaged density thickness for the finite Schmidt number ($Sc = 1$) currents decreases as Re increases, while $\tilde{\delta}_\rho$ of the non-diffusive currents ($Sc \to \infty$) increases with Re. For high-Sc currents, $\tilde{\delta}_\rho$ remains very small for Reynolds numbers up to 10^3. The corresponding density thickness of the finite Schmidt number currents at low Reynolds numbers is significantly larger. With increasing the Reynolds number, the ratio between the time-averaged density thickness of the $Sc = 1$ current and that of the $Sc \to \infty$ current ($\tilde{\delta}_\rho(Sc = 1)/\tilde{\delta}_\rho(Sc \to \infty)$) sharply decreases and reaches a value of about 1.3 at $Re = 10^4$. The $O(1)$ value of $\tilde{\delta}_\rho(Sc = 1)/\tilde{\delta}_\rho(Sc \to \infty)$ suggests that convective mixing is significant in the high Reynolds number regime. Therefore, Fig. 7 indicates that the interfacial layer is less sensitive to the Schmidt number variations at high Re. However, molecular diffusion still has a quantifiable effect in high-Re low-Sc currents, since $\tilde{\delta}_\rho$ is 30% larger in the diffusive currents than in the non-diffusive currents. The manifestation of diffusion is also observable through the slight increase in $\tilde{\delta}_\rho$ with time for the $Sc = 1$ high-Re current, as observed in the inset of Fig. 7.

Fig. 6 Contours of $\tilde{\rho}$ at $\tilde{t} = 12.7$ of density currents for varying Re. Results with $Sc = 1$ and $Sc \to \infty$ are from the spectral method and finite-volume method, respectively. **a** $Re = 10^4$; **b** $Re = 10^3$; **c** $Re = 317$; **d** $Re = 10^2$. For each Re, the upper (*bottom*) picture corresponds to currents of $Sc = 1$ ($Sc \to \infty$). The values of the plotted contours are $\tilde{\rho} = 0.05 - 0.275 - 0.5 - 0.725 - 0.95$. Images are vertically stretched by a factor 3.33

Pawlak and Armi [30] studied the spatially developing region of a steady downslope current in transition from hydraulically controlled wedge. This configuration is quite different from ours and thus a direct comparison with the present results is not fruitful. However, in order to verify that conclusions drawn from the analysis of the density thickness are insensitive to the choice of the indicator chosen to quantify mixing, we also compute $\tilde{\vartheta}_\rho$ as a simple measure of mixing volume fraction,

$$\tilde{\vartheta}_\rho = \frac{1}{2Hx_F} \int_0^H \int_0^L F(\tilde{\rho}) \mathrm{d}x \mathrm{d}z, \tag{3.2}$$

where F is a box filter defined as $F(\tilde{\rho}) = \{1 \text{ if } \beta \leq \tilde{\rho} \leq 1 - \beta\,;\ 0 \text{ otherwise}\}$. Here β is a small threshold taken to be equal to 0.01, and $\tilde{\vartheta}_\rho$ is scaled by the volume $2Hx_F$, which represents the portion of the channel crossed by the current at the time considered. Figure 7 also shows $\tilde{\vartheta}_\rho$ plotted for currents of varying Re and Sc and the behavior is very close to that of $\tilde{\delta}_\rho$.

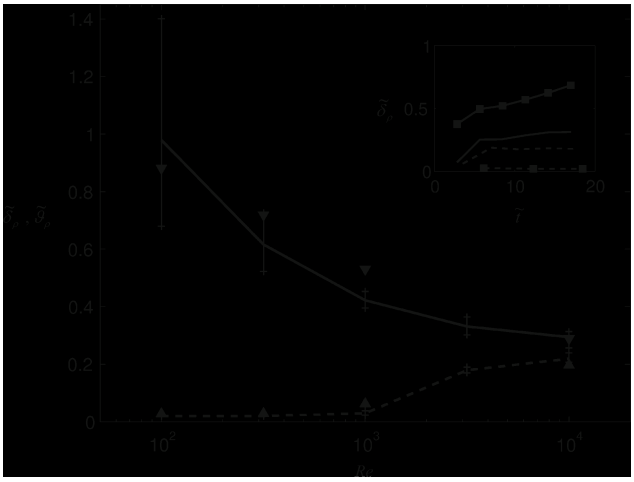

Fig. 7 Evolution of the time-averaged density thickness $\tilde{\delta}_\rho$ with the Reynolds number. *Solid line:* $Sc = 1$. *Dashed line:* $Sc \to \infty$. The *error bars* represent the range of variation in $\tilde{\delta}_\rho$ during $8 \leq \tilde{t} \leq 20$. The *inset* shows the temporal evolution of $\tilde{\delta}_\rho$ at $Re = 10^4$ (*without symbol*) and $Re = 317$ (*squares*), and $Sc = 1$ (*solid lines*) and $Sc \to \infty$ (*dashed lines*). For comparison we also plot the evolution of $\tilde{\vartheta}_\rho$ (Eq. 3.2) for $Sc = 1$ (*downward triangles*) and $Sc \to \infty$ (*upward triangles*)

3.2 Characteristics of the head

Several high-resolution spectral simulations of density currents with $Sc = O(1)$ have been performed during the last decade [3,9,13,18,25,29]. However to our knowledge, simulations of high-Sc density currents have been rare. In the following we analyse the shape of the head of high-Sc density current for varying Reynolds number.

The shape of the head of the density current for four different Re is shown in Fig. 6. At low Reynolds numbers, the current head is differentiated from the body by a pronounced depression. This is a feature of the high Schmidt number as it is not observed at $Sc = O(1)$. We observe that this depression is not stationary and that its existence is dependent on Re. It is observed only at low and moderate Reynolds numbers. At low Reynolds numbers ($Re \leq O(10^2)$) the surface depression gradually moves from the lock position to the head of the current and eventually shrinks (see the position of the depression just before shrinkage, in the lower snapshot of Fig. 6d; the depression reaches the front at $\tilde{t} \approx 14$ in this case). At high Reynolds numbers ($Re \geq O(10^4)$), Kelvin–Helmholtz instabilities grow rapidly and the vortex structures have moved sufficiently close to the head that a clear independent surface depression is not observable anymore. Interestingly, in the intermediate Re range the depression is still present but, after traveling to the vicinity of the front, the depression exhibits a periodic evolution. As can be seen in Fig. 8, the depression successively grows, gets detached from the body of the current and results in a small blob of low density fluid which is entrained into the high density head (a similar symmetric behavior is observed at the other end in the head of the light front). Note that during this process, the length of the head progressively decreases while the height remains roughly constant. Owing to near immiscibility, the light fluid does not quickly mix with the surrounding heavy fluid. This scenario is repeated as long as the current spreads forward, resulting in complex strands of unmixed fluid entrained into the current head.

3.3 Roll-up of the interface

An interesting observation that can be made in Fig. 6 for $Re = 10^3$ is that while the interface for the high-Sc current remains stable, instability and coherent vortex structures are observed for the $Sc = 1$ current. This indicates the dependence of local Richardson number defined as $Ri = -g(\partial\rho/\partial z)/(\rho(\partial u/\partial z)^2)$ on the Schmidt number [14]. Here, $\partial u/\partial z$ is the local vertical gradient of the streamwise velocity component and $\partial\rho/\partial z$ is the corresponding density gradient. We can consider both the high- and low-Sc density currents to experience roughly a similar magnitude of shear (see Fig. 9 for a quantitative comparison). However, the interface is sharper and the density gradient across the interface is higher in the $Sc \to \infty$ case. Therefore, the stabilizing effect of stratification is expected to be stronger.

Fig. 8 Time evolution of the current head for the $Sc \to \infty$, $Re = 10^3$ case. The first snapshot is at $\tilde{t} = 13$ and the time interval between successive views is $\Delta\tilde{t} = 1.6$ (reading from *top* to *bottom*)

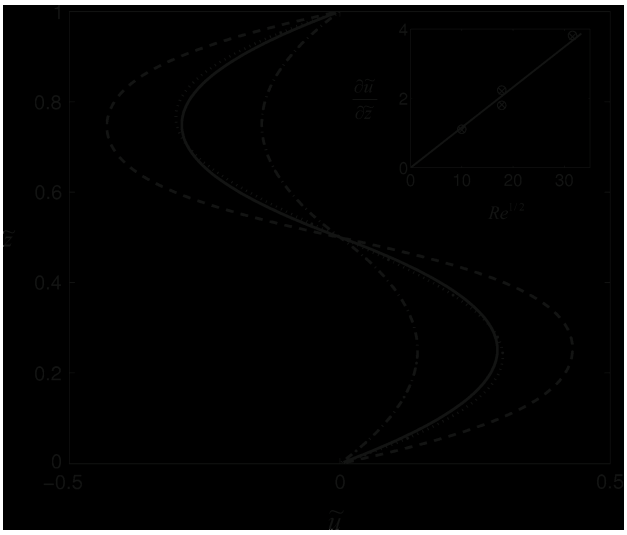

Fig. 9 Velocity profiles for the various *Sc* and *Re* cases, at $\tilde{t} = 12.7$ and at location $\tilde{x} = \tilde{x}_0$. *Dashed-dotted line:* $Sc \to \infty$, $Re = 10^2$; *solid line:* $Sc \to \infty$, $Re = 317$; *dashed line:* $Sc \to \infty$, $Re = 10^3$; *dotted line:* $Sc = 1$, $Re = 317$. Note that the profiles of the $Sc = 1$ and $Sc \to \infty$ currents almost superimpose. The inset shows the variation of the velocity gradient with the Reynolds number (the gradients are computed at the $\tilde{z}$-location corresponding to the position of the inflexion point in the velocity profiles). *Circles* correspond to velocity gradients computed from velocity profiles located at $\tilde{x} = \tilde{x}_0$ and crosses correspond to velocity gradients computed at $\tilde{x} = \tilde{x}_0 + 1.25$. Note that the results are independent of the choice of $\tilde{x}$

In the following, we attempt to obtain an estimate of the Richardson number based on the global parameters of the flows. The analysis will be more general for currents of arbitrary density ratio, and not limited to Boussinesq currents. For this purpose, we choose the velocity scaling to be $\sqrt{g\,At\,H}$, where the Atwood number is defined as $At = (\rho_H - \rho_L)/(\rho_H + \rho_L)$. This rescaling allows the characteristic velocity to remain finite at high density ratio. In the limit $At \to 1$, the characteristic velocity reduces to $\sqrt{gH}$, which is of the same order of magnitude as that predicted by the shallow-water theory for the dam-break problem [31]. Rewriting Richardson number in non-dimensional terms,

$$Ri = \frac{-\left(\partial\tilde{\rho}/\partial\tilde{z}\right)}{\left(\partial\tilde{u}/\partial\tilde{z}\right)^2}\frac{1}{\left(1-At\right)/2 + At\,\tilde{\rho}}. \tag{3.3}$$

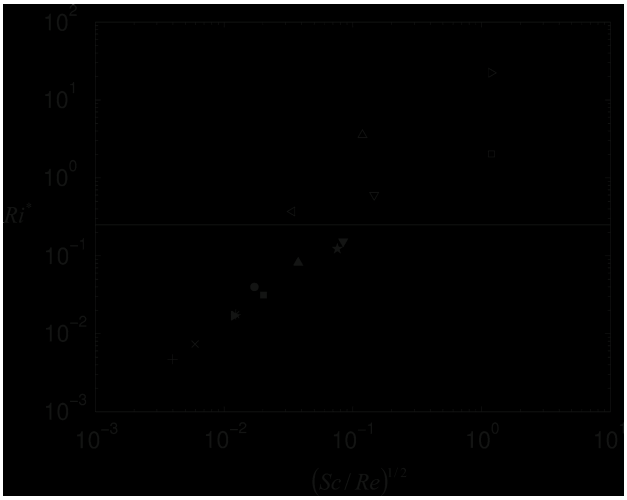

Fig. 10 Ri^* computed as in (3.5) versus $\sqrt{Sc/Re}$ for the numerical and experimental data detailed in Table 2. The *solid line* is the criterion $Ri^* = 0.25$

Estimating the density gradient to be $\partial\tilde{\rho}/\partial\tilde{z} \sim (ScRe)^{1/2}$, and the velocity gradient to be $\partial\tilde{u}/\partial\tilde{z} \sim (\tilde{u}_H + \tilde{u}_L)$ $Re^{1/2}$($\tilde{u}_H$ and $\tilde{u}_L$ being the generalized non-dimensional velocities of the heavy and light fronts), the Richardson number can be expressed as

$$Ri \sim \frac{1}{(\tilde{u}_H + \tilde{u}_L)^2}\sqrt{\frac{Sc}{Re}}\frac{2}{(1-At) + 2At\,\tilde{\rho}}. \tag{3.4}$$

The estimate for the velocity gradient is verified in Fig. 9 in which the vertical velocity profiles at the center of the currents ($\tilde{x} = \tilde{x}_0$) are plotted for the different Re and Sc cases. The evolution of the corresponding non-dimensional velocity gradient, measured at the interface is plotted in the inset as a function of $Re^{1/2}$. It is observed that, in agreement with the aforementioned scaling, velocity gradient is nearly independent of the Schmidt number, and is proportional to the square-root of the Reynolds number. The estimate of the velocity gradient has been repeated at other horizontal locations within the current and the results are insensitive to the actual choice of location.

In the limit of a Boussinesq current ($At \to 0$), Richardson number is independent of the precise value of $\tilde{\rho}$, while in the limit of large contrast ($At \to 1$) Ri varies as $1/\tilde{\rho}$. In order to get an estimate of the bulk Richardson number that is independent of the precise location inside the current, we assume $\tilde{\rho} \sim 0$ in Eq. (3.4), and define a *bulk Richardson number* Ri^* as follows,

$$Ri^* \equiv \frac{1}{(\tilde{u}_H + \tilde{u}_L)^2}\sqrt{\frac{Sc}{Re}}\frac{2}{1-At}. \tag{3.5}$$

We plot in Fig. 10 the value of Ri^* corresponding to various computed density currents as a function of $(Sc/Re)^{1/2}$. Also included are the numerical and experimental results of Härtel et al. [18], Cantero et al. [8] for Boussinesq currents, and Birman et al. [3] and Lowe et al. [26] for non-Boussinesq currents of density ratio 2.5. In all these cases Sc, Re, $\tilde{u}_H$ and $\tilde{u}_L$ are known and these values are presented in Table 2. All the density currents reported by the aforementioned authors exhibit strong vortex structures.

For parallel flows of a stratified fluid, there exist a local stability threshold, $Ri_C = 0.25$, below which Kelvin–Helmholtz instabilities are amplified [11,14]. It is observed that all the currents observed to be unstable (*resp.* stable) have a Ri^* below (resp. above) the critical value of $Ri_C = 0.25$. Therefore the threshold $Ri_C = 0.25$ appears to provide a good estimate of interfacial instability and roll up in gravity currents when used in conjunction with the bulk Richardson number Ri^*.

3.4 Front velocity

Here we examine the influence of the Schmidt number on the front velocity of the density currents. The velocity of the front, scaled by $\sqrt{g'H}$, is computed as $\tilde{u}_F = \left|\mathrm{d}\tilde{x}_F/\mathrm{d}\tilde{t}\right|$. The front position $\tilde{x}_F$ is determined as the

Table 2 Data used in Fig. 10 to study the stability of the interface of gravity currents

Reference	Legend	Type of data	Sc	ρ_H/ρ_L	$\tilde{u}_L$	$\tilde{u}_H$	Re
Unstable interface							
Lowe et al. [26]	★	Experiments	≈ 700	1.47	0.380	0.404	1.92×10^5
Birman et al. [3]	●	2D-spectral	1	2.5	0.266	0.392	6.325×10^3
Härtel et al. [18]	×	2D-spectral	0.71	≈ 1	0.460	0.460	1.26×10^5
Härtel et al. [18]	+	2D-spectral	0.71	≈ 1	0.450	0.450	5.66×10^4
Härtel et al. [18]	■	3D-spectral	0.71	≈ 1	0.403	0.403	3.464×10^3
Cantero et al. [8]	✳	3D-spectral	0.71	≈ 1	0.424	0.424	8.945×10^3
Present study	▶	2D-spectral	1	≈ 1	0.423	0.423	10^4
Present study	▲	2D-spectral	1	≈ 1	0.339	0.339	10^3
Present study	▼	2D-spectral	5	≈ 1	0.372	0.372	10^3
Stable interface							
Present study	◁	2D-spectral	1	≈ 1	0.212	0.212	3.17×10^2
Present study	△	2D-spectral	1	≈ 1	0.091	0.091	10^2
Present study	▽	2D-spectral	5	≈ 1	0.250	0.250	3.17×10^2
Present study	▷	2D-spectral	100	≈ 1	0.115	0.115	10^2
Present study	□	2D-finite-volume	$O(10^3)$[a]	1.01	0.384	0.384	10^3

The front velocities of the present results are measured at $\tilde{t} = 20$. Here velocity is scaled by $\sqrt{g\varepsilon H}$, and Re is defined as in Eq. (2.8). According to the velocity scaling used in Sect. 3.3, the value of $\tilde{u}_L$ and $\tilde{u}_H$ are to be multiplied by $(1 + \rho_H/\rho_L)^{1/2}$, and Re is to be multiplied by $(1 + \rho_H/\rho_L)^{-1/2}$ in order to obtain the values of Ri^* and $\sqrt{Sc/Re}$ plotted in Fig. 10

[a] We used the value $Sc = 10^3$ as estimated in Appendix, for the finite-volume method ($Sc \to \infty$)

location where the vertically integrated dimensionless height of the current, $\tilde{h}$, becomes smaller than a small threshold $\delta = 0.01$ (see Cantero et al. [8] for a discussion of the choice of this parameter). Here $\tilde{h}$ is defined as [3,27,34],

$$\tilde{h}\left(\tilde{x}, \tilde{t}\right) = \int_0^1 \tilde{\rho}\, d\tilde{z}. \tag{3.6}$$

As the current spreads it goes through acceleration, slumping, inertial and viscous phases of evolution [23]. In the slumping phase, the planar current moves at a nearly constant speed. Provided Re is sufficiently large, the flow then enters an inertial self-similar phase of deceleration [32], in which the current moves under the balance of buoyancy and inertial forces [20,23]. The speed of the planar gravity current in this inertial phase evolves as $t^{-1/3}$ [15]. At later times, when viscous effects become important the current transitions to the viscous phase [20,21]. Based on shallow-water theory, two rate of spreading have been proposed depending on the nature of the dominant friction. If the viscous effects are primarily due to the interface shear, u evolves as $t^{-5/8}$ [20]. If they are primarily due to the friction at the bottom wall, u evolves as $t^{-4/5}$ [21].

Figure 11 shows the temporal evolution of the front velocity of the low-Re Boussinesq currents displayed in Fig. 5. The front velocity continuously increase from the lower curve for the low Schmidt number case ($Sc = 1$) to the upper curve for the non-diffusive case ($Sc \to \infty$). In the low Schmidt number cases after an initial acceleration phase that extends for about one dimensionless time unit the front velocity smoothly decreases.

In the case of highly miscible fluids (low-Sc) at low Reynolds numbers the question of how to define appropriately the front location and its velocity arises [7]. As can be observed in Figs. 5 and 6, the width of the front as indicated by the different density contours is quite thick for $Sc = 1$ at $Re = 10^2$. The definition of the front location and as a result the front velocity become strongly dependent on the value of $\tilde{\rho}$ used in demarking the two fluids. With increasing the Reynolds number contours of $\tilde{\rho}$ close to 0 cluster at the heavy front and those close to 1 cluster at the light front, thus reducing the uncertainty in clearly defining a front location. The dominant role of diffusion at low Re can be quantified. Under pure diffusion, the thickness of the interface between two miscible fluids can be estimated to increase with time as $\sqrt{\tilde{t}/ScRe}$. Figure 12 displays the front velocity, $\tilde{u}_\alpha$, of the heavy current as identified by the time evolution of the velocity of the most forward position of the contour $\tilde{\rho} = \alpha$ in the lower half of the domain, for three different values of $\alpha = 0.05$, 0.5 and 0.95 for the case of $Re = 10^2$ and $Sc = 1$. Also plotted in the figure are lines corresponding to $\pm 1/\sqrt{ScRe\,\tilde{t}}$. At very early times ($\tilde{t} \leq 1$) buoyancy dominates and the front as identified by all three contours propagate forward in

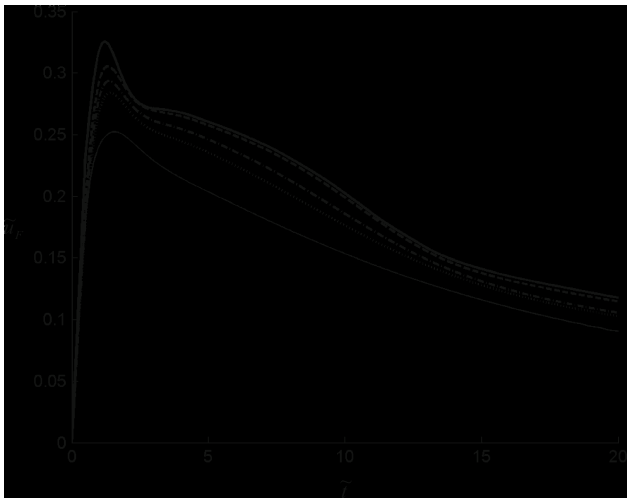

Fig. 11 Time evolution of the front velocity ($Re = 10^2$) for varying Sc. *Thin solid line:* $Sc = 1$; *dotted line:* $Sc = 5$; *dashed-dotted line:* $Sc = 10$; *dashed line:* $Sc = 10^2$; *thick solid line:* $Sc \to \infty$. Computations of $Sc = 1, 5, 10$ and 10^2 are with the spectral code while the computation of $Sc \to \infty$ current is with the finite-volume code. The spatial resolutions are the same as in Fig. 5

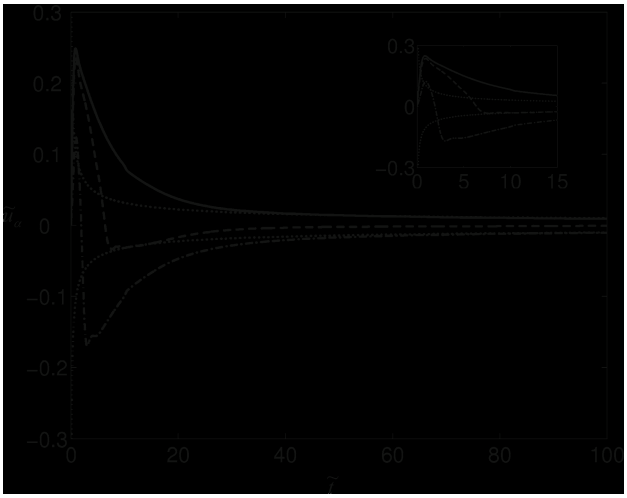

Fig. 12 Time evolution of the front velocity, $\tilde{u}_\alpha$, of the heavy current as identified by the velocity of the most forward position of the contour $\tilde{\rho} = \alpha$ in the lower half of the domain, for three different values of α for the case of $Re = 10^2$ and $Sc = 1$. Time evolution of $\tilde{u}_\alpha$ of some density contours $\tilde{\rho} = \alpha$ in a diffusive current ($Sc = 1$, $Re = 10^2$). *Solid line:* $\alpha = 0.05$; *dashed line:* $\alpha = 0.5$; *dash-dotted line:* $\alpha = 0.95$. The *dotted lines* represent $\pm 1/\sqrt{Sc\ Re\ \tilde{t}}$. At late times, the spreading of the interface is mostly due to diffusive effect

the same direction as dictated by the pressure gradient. After this short phase of acceleration, diffusive effects become significant and the contours decelerate accordingly ($1 \leq \tilde{t} \leq 8$) to eventually spread as a dominantly diffusive interface ($\tilde{t} \geq 20$).

The behavior for the high-Sc currents is somewhat more complicated (upper curves in Fig. 11). Even with the numerical diffusion [estimated as an effective Schmidt number of $O(10^3)$], the above effect of diffusion on the smearing of the interface is more than an order of magnitude weaker. For the $Sc \to \infty$ case, following the initial acceleration and deceleration, a tendency towards a constant velocity slumping phase can be observed ($3 \leq \tilde{t} \leq 4$). The Reynolds number at release is sufficiently low that transition from slumping to viscous phase occurs early without any inertial phase in between. In Fig. 11 the time evolution of front velocity exhibits an inflection point for the high-Sc currents at $\tilde{t} \approx 14$. This time corresponds to the time at which the depression reaches the front of the density current (not shown here).

In Fig. 13, the time evolution of front velocities is plotted for currents of $Re = 10^2$, 317, 10^3 and 10^4. The thin and thick lines correspond to density currents of $Sc = 1$ and $Sc \to \infty$, respectively and the behavior

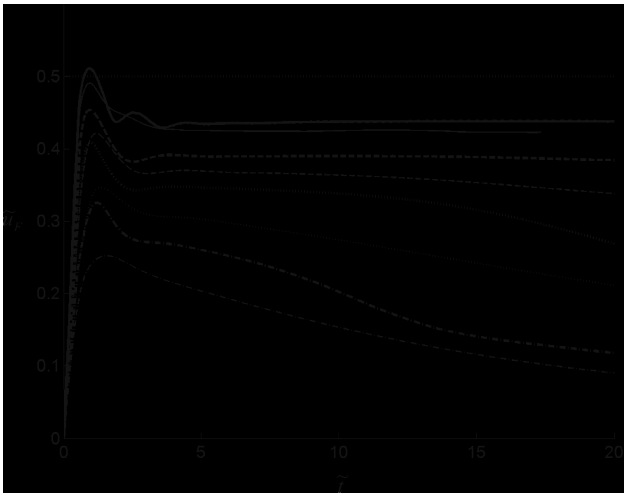

Fig. 13 Time evolution of the front velocity of density currents of various Schmidt number and Reynolds number. The *thick* and *thin lines* correspond to density currents of $Sc \to \infty$ and $Sc = 1$, respectively. *Dashed-dotted lines:* $Re = 10^2$; *dotted lines:* $Re = 317$; *dashed lines:* $Re = 10^3$; *solid lines:* $Re = 10^4$. The *horizontal dotted line* is Benjamin [2] prediction. The spatial resolutions are the same as in Fig. 6

for all other intermediate Schmidt numbers is bounded in between. The velocity difference between the low- and high-Sc currents continuously decreases as Re increases. For instance, the velocity difference at $\tilde{t} \approx 5.7$ is 23.0, 13.3, 5.4 and 2.3% for $Re = 10^2$, 317, 10^3 and 10^4, respectively. With increasing Re the transition to viscous phase is observed to be delayed. The front velocity steadily increases with increasing Re and even at the largest Reynolds number considered the front velocity is noticeably lower than the theoretical prediction of Benjamin [2]. It may be argued that in reality the coherent vortices observed upstream of the front may undergo instability and become three-dimensional, which might influence the velocity of the front. It has been shown that in the slumping phase the speed of the current is nearly the same in both two-dimensional and three-dimensional simulations [9]. Clearly the finite $O(1)$-value of the Schmidt number often employed in such computations is not the source of discrepancy, since even the front velocity of the non-diffusive current is lower than the theoretical limit. The difference is in the use of no-slip boundary conditions. Instead if free-slip boundary conditions are employed the theoretical limit is approached to within 2% in the steady slumping phase at sufficiently large Re [18].

3.5 Effect on three-dimensionality

We now proceed to address the effect of the Schmidt number on the onset of three-dimensional structures observed in both experimental and computed density currents [8,18,35]. We first perform a three-dimensional computation of the lock–exchange flow under the same conditions as in Fig. 2 of Härtel et al. [18], i.e. at $Re = 3464$. The only difference is that while Härtel et al. [18] imposed $Sc = 0.71$, here we consider a non-diffusive current of $Sc \to \infty$ and thus the role of three-dimensionality of the current can be ascertained. We use a modest grid of $480 \times 60 \times 80$ points along the streamwise, spanwise and wall-normal directions (x, y, z) with a domain of size $15H \times 1.5H \times H(L = 15H)$. This resolution is equivalent to that used in Fig. 3a and is sufficient to accurately capture the essential large-scale instabilities and features of the flow. Free-slip boundary conditions are imposed along the streamwise boundaries, no-slip conditions are enforced along the top and bottom walls and periodic conditions are imposed along the spanwise direction. The flow is started from rest and a small random disturbance is superimposed on the density field. Note that with the present grid, the total variation of the overall mechanical energy, due to numerical dissipation stemming from spatial discretization, is less than 0.02% during the entire duration of the simulation.

At low Sc, Härtel et al. [18] and Cantero et al. [8] observed instabilities at the bottom foremost part of the current and the instability grows rapidly to form a pattern of lobes and clefts. They also observed three-dimensional vortex structures along the body of the current due to three-dimensional instabilities of the Kelvin–Helmholtz vortices at the interface between the light and heavy fluid. Figure 14 shows the time evolution of three-dimensionality as visualized by a surface of constant density ($\tilde{\rho} = 0.5$). The vortex structures

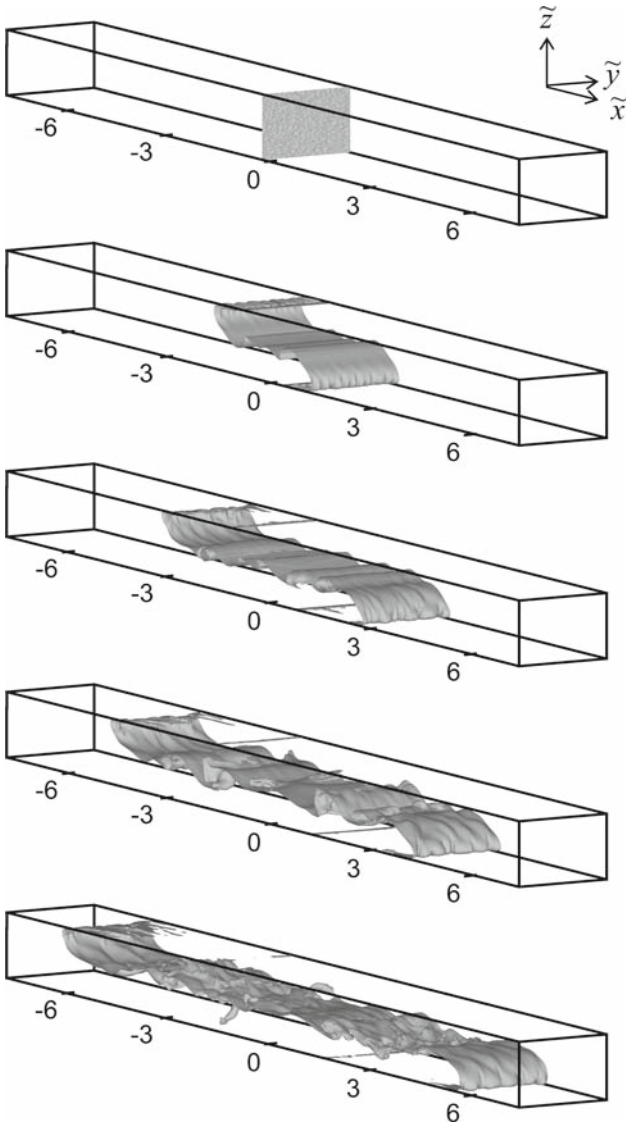

Fig. 14 Three-dimensional high-Sc Boussinesq density current in lock–exchange configuration at $Re = 3464$ and $Sc \to \infty$ (visualization of the surface $\tilde{\rho} = 0.5$). Time interval between successive views is $\Delta\tilde{t} = 5$. The size of the $(\tilde{x}, \tilde{y}, \tilde{z})$ domain is $15 \times 1.5 \times 1$

at the interface along the body of the current are somewhat smaller than the ones reported for $O(1)$ Schmidt number by the aforementioned authors. We can see the lobe and cleft pattern at the head of the current. Härtel et al. [18] and Cantero et al. [8] reported a non-dimensional front velocity of 0.403 for the $O(1)$ Schmidt number case, while we observe a velocity of 0.417 for the present high-Sc current. The difference is small and is less than 3.5%. As already mentioned in Sect. 3.4, this confirms that the front velocity is only weakly dependent on Sc at sufficiently high Re.

Härtel et al. [19] performed a linear stability analysis of the flow at the head of a low-Sc two-dimensional density current for a wide range of Re ($10^2 \leq Re \leq 1.4 \times 10^4$). They were able to predict the spanwise wavelength, λ, of the most unstable three-dimensional instability responsible for the formation of lobe and cleft pattern. For instance, they obtained $\lambda = 0.157H$ at $Re \approx 2830$. From Fig. 14, we can estimate the wavelength of the lobe and cleft instability by counting the number of lobes over time. The number of lobes is observed to remain approximately constant and equal to 10 over the period $\tilde{t} = 5$ to $\tilde{t} = 10$. This leads to an estimated spanwise wavelength of $\lambda = 0.15H$, which is in good agreement with the finite $O(1)$ Schmidt number result of $0.157H$. We also performed similar analysis for currents of different Reynolds number, namely $Re = 10^3$

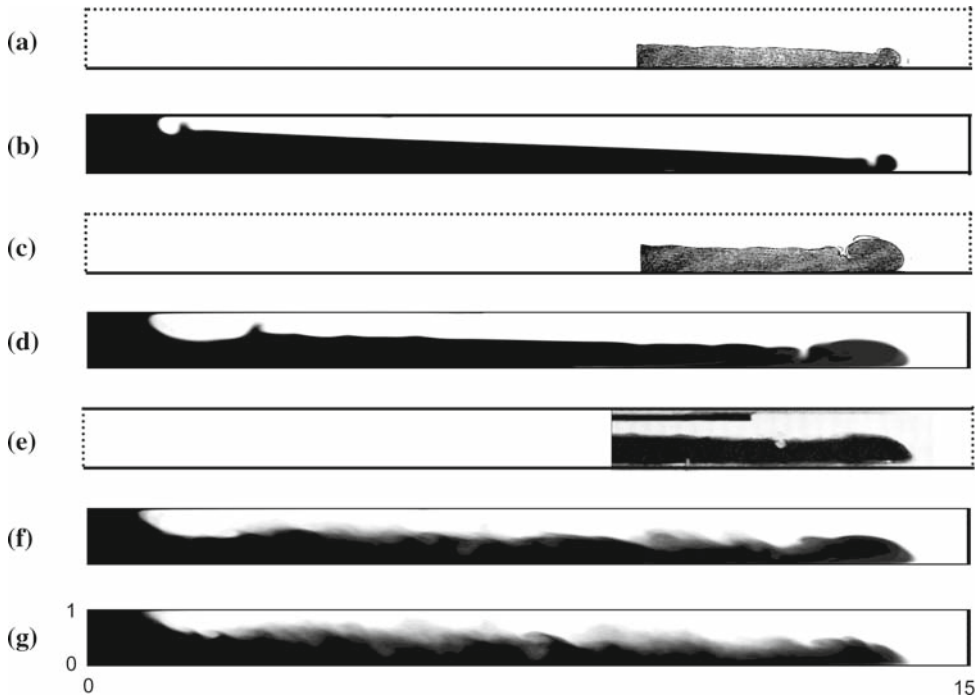

Fig. 15 Shadowgraph images of moderate to high-*Sc* gravity currents. **a,c** From the experiments of Schmidt [33]; **b, d, f, g** from the present three-dimensional computations with the finite volume method ($Re = 317$, 10^3, 3,464 and 10^4, respectively); **e** from the experiments of Thorpe [37] at $Re \approx 2970$. In frames (**a**) and (**c**) the current is due to temperature differences of $\Delta T = 0.5°\text{C}$ and 1.5°C in air, respectively. In **e** the current is due to a density difference in salted water of $\Delta\rho = 3.34 \times 10^{-2}\text{gm/cm}^3$. In **b, d, f, g** the density field is averaged along the spanwise direction and the grid resolution is the same as in Fig. 14. Snapshots **b, d, f, g** show the currents at a time when the current has advanced about $6H$. Fictitious boundaries are added in **a, c, e** for clarity, *dotted lines* are used when the position of the actual boundary is unknown

and $Re = 10^4$, and similar agreement with $O(1)$ Schmidt number cases is observed. This indicates that the underlying mechanisms responsible for the lobe and cleft formation are relatively insensitive to the Schmidt number.

Figure 15 shows qualitative evolution of the topology of moderate to high-*Sc* density currents with the Reynolds number. The results shown are obtained from the present three-dimensional simulations, which are compared against the experimental data of Schmidt [33] and Thorp [37]. In Schmidt's experiments the density variation is due to temperature difference in air, so the estimated Schmidt number is approximately 0.7. However, the precise conditions of the experiments are not known, therefore comparison is only qualitative. In Thorpe's experiments the density variation is due to salt in water, leading to a Schmidt number of 700 approximately, and the Reynolds number is 2,970. In general, qualitative agreement is observed between present simulations and above experiments. For example, at the lowest *Re* considered the gentle slope of the interface with a pronounced depression that separates the body from the head can be observed both in the experimental and the computational results. The depression can be observed at the intermediate Reynolds number as well, however, the head of the current has grown in size and the body of the current shows small undulations, which can be observed both in the experimental and computational results. At the highest Reynolds number shown the interface is turbulent. Since the flow is three dimensional, frames (f) and (g) show span-averaged results. When compared with the corresponding two-dimensional results shown in figure 6a, the effect of three-dimensionality is clear. The strong coherent Kelvin–Helmholtz vortices at the interface are broken by three-dimensional instability and upon span-average the interface shows a relatively smooth structure. The span-averaged results are in better agreement with the high Reynolds number experimental results of Thorpe [37] and Schmidt [33].

The three-dimensional structure of the current, and in particular the details of the surface depression, is shown in Fig. 16. In line with the observations made for the two-dimensional currents in Figs. 5 and 6, the current head is differentiated from the body by a pronounced surface depression at the lowest Reynolds number under consideration. The depression exhibits some three-dimensionality with small undulation along the spanwise direction. A closer look suggests that the average wavelength of these undulations compared well

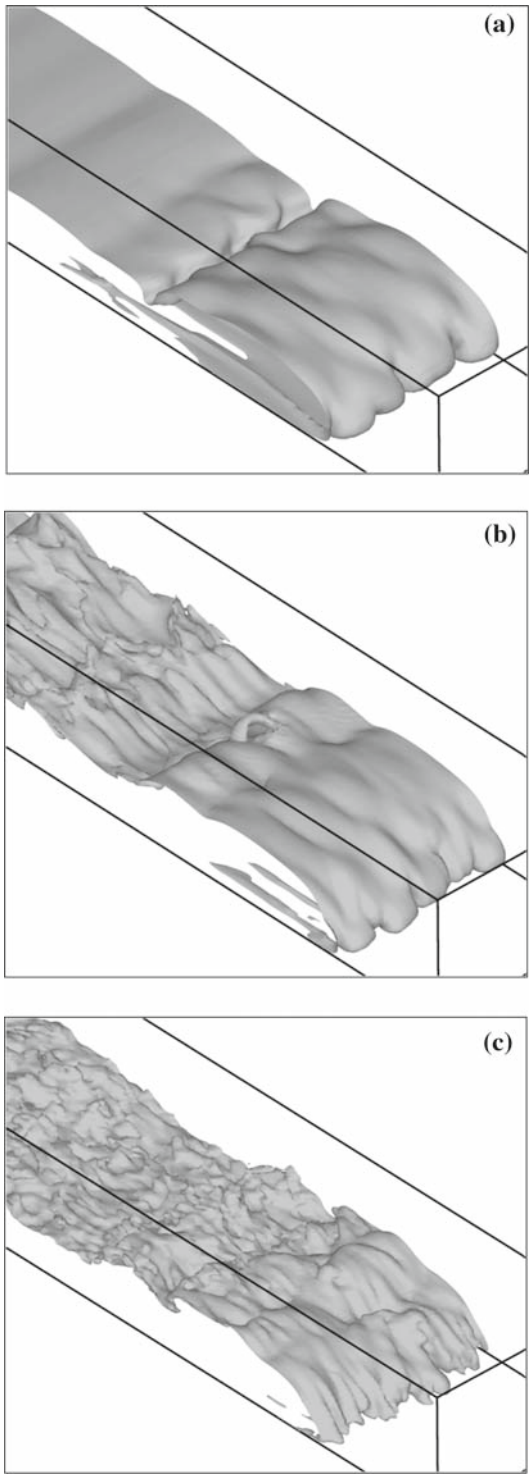

Fig. 16 Three-dimensional structure of the interface in high-*Sc* currents at different *Re* (visualization of the surface $\tilde{\rho} = 0.5$). **a** $Re = 10^3$; **b** $Re = 3464$; **c** $Re = 10^4$. The corresponding time of the snapshots is identical to those in Fig. 15

with that of the lobes and cleft structure formed at the front. Also the spanwise location of the undulation crests and troughs coincide with the location of lobes and clefts. At $Re = 10^3$, three-dimensionality is limited to the head of the current and the body remains relatively flat. At $Re = 3464$, the depression of the interface

that separates the head from the body is still visible and its three-dimensionality correlates well with the lobe and cleft structure of the head. The body of the current is however observed to be strongly three dimensional. With further increase in the Reynolds number, the interface takes a fully turbulent structure (Fig. 16c) and the spanwise wavelength of the lobes and clefts decreases, in agreement with the trend found in the stability analysis by Härtel et al. [19]. Furthermore, the head of the current is not well demarcated from the body and strong three-dimensionality can be observed to penetrate right up to the nose of the current.

4 Summary and conclusions

We carried out a numerical investigation of Boussinesq density currents of various Schmidt number and Reynolds number. The goal was to investigate in greater detail the role of Sc on the structure and dynamics of lock–exchange flows. For this purpose we used two complementary approaches, namely a spectral method and a finite-volume interface capturing method that allow us to explore a wide range of Schmidt number $1 \leq Sc \leq \infty$ and Reynolds number $10^2 \leq Re \leq 10^4$.

A quantitative comparison of the size of the mixing region is made. It is observed that at large Reynolds numbers, say $Re \geq O(10^4)$, the size of the mixing region in diffusive and non-diffusive currents is of the same order of magnitude. This confirms that in this regime, mixing that occurs at the interface is mainly due to strong advection generated by the Kelvin–Helmholtz vortices and the smaller scale instabilities. Nevertheless, diffusive effects are still observable in low-Sc currents and account for the somewhat larger size of the mixing region.

In contrast, the size of the mixing region in viscous density currents is strongly dependant on Sc. When diffusion is dominant the thickness of the mixing region has been verified to scale as $(ScRe)^{-1/2}$. Additionally, the Schmidt number is observed to affect the shape of the current head. A depression that separates the head from the body of the current is observed at high-Sc, while such a depression of the interface is not detected at low-Sc. This depression is non-stationary since it can either move along the body of the current, reach the head and eventually shrink or exhibit an oscillatory behavior, depending on the value of the Reynolds number.

Three-dimensional simulations of high-Sc current suggest that the lobes and clefts patterns are relatively independent of the Schmidt number. On the contrary the formation of vortex structures along the body of the currents is observed to be dependent on Sc. We developed a simple definition of a bulk Richardson number Ri^* and observed Kelvin–Helmholtz instabilities at the interface to grow and form coherent vortices only when $Ri^* < 0.25$. Above this threshold interfacial instabilities are suppressed.

The computation of the front velocity of diffusive versus non-diffusive currents reveals that the Schmidt number has only a weak influence on the dynamics of the currents at $Re \geq O(10^4)$. In this regime, the velocity of the front is observed to be almost independent (within a few percent) of Sc in the range $1 \leq Sc \leq \infty$. At low Reynolds number, the velocity of diffusive currents is a strong function of the contour level chosen for defining the interface between the heavy and light fluids. Thus, caution needs to be exercised when comparing results between different computations and experiments of low-Re diffusive currents.

Acknowledgments We acknowledge and thank Jacques Magnaudet for the use of the finite-volume code. The present work benefited from the NSF grant EAR-0609712.

Appendix: estimate of the effective Schmidt number for the finite-volume code

Here we estimate an effective Schmidt number for the present finite-volume method, based on the scaling relation for the interface thickness obtained with the finite Sc simulations. As mentioned in Sect. 2.2.2 the evolution equation for the density solved in the finite-volume code is hyperbolic, but the numerical thickness of the interface is not strictly zero as it is typically resolved over three grid cells [6]. This thickness corresponds to an effective Schmidt number which depends on the degree of spatial resolution.

In order to get an estimate of the effective Schmidt number for the finite volume code, we first establish the scaling law for the interface thickness to be $(ScRe)^{-1/2}$ using the interface data obtained from the finite Schmidt number spectral simulations (Fig. 5a–c, and the upper frame of Fig. 6c). We measure the values of the interface thickness h_α (for two different values of $\alpha = 0.05$ and 0.245) for currents of varying Re and Sc obtained from the spectral simulations. Here h_α is defined as the thickness where $\alpha \leq \tilde{\rho} \leq 1 - \alpha$. The results are plotted in Fig. 17. By fitting the data points, we obtain a direct relation between h_α and Sc. For the present

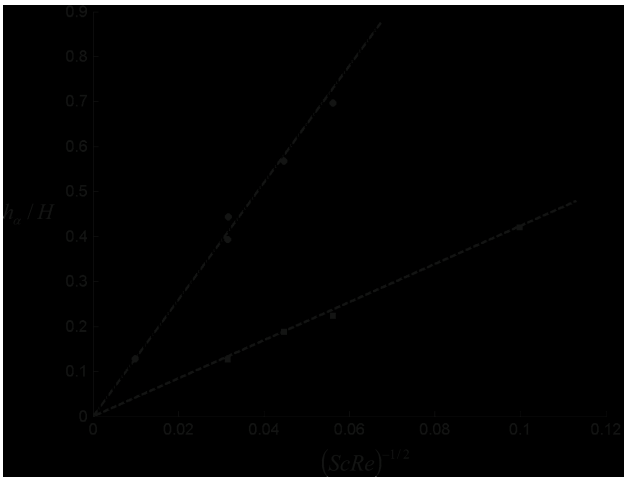

Fig. 17 Variation of h_α with $(ScRe)^{-1/2}$, where h_α is computed at $\tilde{t} = 12.7$. *Circles:* $\alpha = 0.05$; *squares:* $\alpha = 0.275$. The *circles* correspond to currents (in increasing order of h_α) of $Sc = 100, 10, 1, 5, 1$ and $Re = 10^2, 10^2, 10^3, 10^2, 317$, respectively. The *squares* correspond to currents (in increasing order of h_α) of $Sc = 10, 5, 1, 1$ and $Re = 10^2, 10^2, 317, 10^2$, respectively. *Lines* are included to show near linearity

resolution (equivalent to $R2$) we obtain $h_{0.05}/H \approx 13.00 \times (ScRe)^{-1/2}$ and $h_{0.275}/H \approx 4.24 \times (ScRe)^{-1/2}$, respectively.

The numerical thicknesses $h_{0.05}$ and $h_{0.275}$ of the interface for the finite-volume code were then obtained from Fig. 5d. Which, in conjunction with the above scaling relations for the interface thickness, yield effective Schmidt numbers of $Sc \approx 6600$ and 5800 for $\alpha = 0.05$ and $\alpha = 0.275$, respectively. Therefore a conservative estimate of the effective Schmidt number for the present finite-volume method at the present spatial resolution can be estimated to be of $O(10^3)$.

References

1. Allen, J.: Principles of Physical Sedimentology. George Allen and Unwin Ltd., London (1985)
2. Benjamin, T.B.: Density urrents and related phenomena. J. Fluid Mech. **31**, 209–248 (1968)
3. Birman, V., Martin, J.E., Meiburg, E.: The non-Boussinesq lock–exchange problem. Part 2. High-resolution simulations. J. Fluid Mech. **537**, 125–144 (2005)
4. Birman, V.K., Battandier, B.A., Meiburg, E., Linden, P.F.: Lock–exchange flows in sloping channels. J. Fluid Mech. **577**, 53–77 (2007)
5. Bonometti, T., Magnaudet, J.: Transition from spherical cap to toroidal bubbles. Phys. Fluids 18:052102 (2006)
6. Bonometti, T., Magnaudet, J.: An interface-capturing method for incompressible two-phase flows. Validation and application to bubble dynamics. Int. J. Multiph. Flow **33**, 109–133 (2007)
7. Brenner, H.: Kinematics of volume transport. Physica A **349**, 11–59 (2005)
8. Cantero, M., Balachandar, S., Garcia, M., Ferry, J.: Direct numerical simulations of planar and cyindrical density currents. J. Appl. Mech. **73**, 923–930 (2006)
9. Cantero, M.I., Lee, J.R., Balachandar, S., Garcia, M.H.: On the front velocity of gravity currents. J. Fluid Mech. **586**, 1–39 (2007)
10. Canuto, C., Hussaini, M., Quarteroni, A., Zang, T.: Spectral Methods in Fluid Dynamics. Springer, Heidelberg (1988)
11. Chandrasekhar, S.: Hydrodynamic and Hydromagnetic Stability. Clarendon Press, Oxford (1961)
12. Cortese, T., Balachandar, S.: High performance spectral simulation of turbulent flows in massively parallel machines with distributed memory. Int. J. Supercomput. Ap. **9**, 187–204 (1995)
13. Daly, B., Pracht, W.: Numerical study of density-current surges. Phys. Fluids **11**, 15–30 (1968)
14. Drazin, P.G., Reid, W.H.: Hydrodynamic Stability, 2nd edn. Cambridge University Press, Cambridge (1981)
15. Fay, J.: The spreads of oil slicks on a calm sea. In: Hoult, D.P. (ed.) Oils in the Sea, pp. 53–63. Plenum Press, New yorkm (1969)
16. Grant, G.B., Jagger, S.F., Lea, C.J.: Fires in tunnels. Philos. Trans. R. Soc. Lond. A **356**, 2873–296 (1998)
17. Gröbelbauer, H.P., Fanneløp, T.K., Britter, R.E.: The propagation of intrusion fronts of high density ratio. J. Fluid Mech. **250**, 669–687 (1993)
18. Härtel, C., Meiburg, E., Necker, F.: Analysis and direct numerical simulation of the flow at a gravity-current head. Part 1. Flow topology and front spedd for slip and no-slip boundaries. J. Fluid Mech. **418**, 189–212 (2000a)
19. Härtel, C., Carlsson, F., Thunblom, M.: Analysis and direct numerical simulation of the flow at a gravity-current head. Part 2. The lobe-and-cleft instability. J. Fluid Mech. **418**, 213–229 (2000b)
20. Hoult, D.: Oil spreading in the sea. Annu. Rev. Fluid Mech. **4**, 341–368 (1972)

21. Huppert, H.: The propagation of two-dimensional and axisymmetric viscous density currents over a rigid horizontal surface. J. Fluid Mech. **121**, 43–58 (1982)
22. Huppert, H.E.: Density currents: a personnel perspective. J. Fluid Mech. **554**, 299–322 (2006)
23. Huppert, H., Simpson, J.: The slumping of gravity currents. J. Fluid Mech. **99**, 785–799 (1980)
24. Joseph, D., Renardy, Y.: Fundamentals of Two Fluids Dynamics. Part II. Springer, Heidelberg (1992)
25. Klemp, J.B., Rotunno, R., Skamarock, W.C.: On the dynamics of density currents in a channel. J. Fluid Mech. **269**, 169–198 (1994)
26. Lowe, R.J., Rottman, J.W., Linden, P.F.: The non-Boussinesq lock–exchange problem. Part 1. Theory and experiments. J. Fluid Mech. **537**, 101–124 (2005)
27. Marino, B., Thomas, L., Linden, P.: The front condition for density currents. J. Fluid Mech. **536**, 49–78 (2005)
28. Necker, F., Härtel, C., Kleiser, L., Meiburg, E.: Mixing and dissipation in particle-driven density currents. J. Fluid Mech. **545**, 339–372 (2005)
29. Ozgökmen, T., Fischer, P., Duan, J., Iliescu, T.: Three-dimensional turbulent bottom density currents from a high-order nonhydrostatic spectral element model. J. Phys. Oceanogr. **34**, 2006–2026 (2004)
30. Pawlak, G., Armi, L.: Mixing and entrainment in developing stratified currents. J. Fluid Mech. **424**, 45–73 (2000)
31. Ritter, A.: Die fortplanzung der wasserwellen. Z. Verein. Deutsch. Ing. **36**, 947–954 (1892)
32. Rottman, J., Simpson, J.: Density currents produced by instantaneous releases of a heavy fluid in a rectangular channel. J. Fluid Mech. **135**, 95–110 (1983)
33. Schmidt, W.: Zur Mechanik der boen. Z. Meteorol. **28**, 355–362 (1911)
34. Shin, J., Dalziel, S., Linden, P.: Density currents produced by lock exchange. J. Fluid Mech. **521**, 1–34 (2004)
35. Simpson, J.: Effect of the lower boundary on the head of a gravity current. J. Fluid Mech. **53**, 759–768 (1972)
36. Simpson, J.: Density Currents, 2nd edn. Cambridge University Press, Cambridge (1997)
37. Thorpe, S.A.: A method of producing a shear flow in a stratified fluid. J. Fluid Mech. **32**, 693–704 (1968)
38. von Karman, T.: The engineer grapples with nonlinear problems. Bull. Am. Math. Soc. **46**, 615–683 (1940)
39. Zalesak, S.T.: Fully multidimensional flux-corrected transport algorithms for fluids. J. Comput. Phys. **31**, 335–362 (1979)